Design of morphing winglets with the inclusion of nonlinear aeroelastic effects

R. De Breuker **M. Abdalla** **Z. Gürdal**
r.debreuker@tudelft.nl
Aerospace Structures and Computational Mechanics
Delft University of Technology
Delft, The Netherlands

ABSTRACT

A nonlinear aeroelastic model capable of assessing arbitrary morphing manoeuvres and calculating the associated morphing energy requirement is presented in this paper. The aeroelastic model consists of a close coupling between a corotational beam element, accounting for geometric nonlinearities, and a Weissinger method aerodynamic model, containing the Prandtl-Glauert correction for high-subsonic Mach numbers. The morphing deformations are discretised into three distinct morphing modes; fold morphing, twist morphing, and shear morphing, because of which virtually any morphed shape can be achieved, given a proper distribution of the three modes over the wing. The proposed aeroelastic morphing framework is used to design morphing winglets, and it has been shown that morphing winglets can improve the performance of fixed winglets significantly for regional airliners.

NOMENCLATURE

a_{ij}	aerodynamic influence coefficient
$\mathbf{B}$	transformation matrix
c	deformed chord direction
c_0	undeformed chord direction
$\mathbf{C}$	constitutive matrix
$C_{D;v}$	viscous drag coecient
C_L	lift coefficient
D_i	induced drag
$E_{fs,t}$	folding, shearing, twisting actuation energy
$\mathbf{f}$, $\mathbf{f_a}$	structural, aerodynamic force vector
GA	shearing stiffness
GJ	warping stiffness
$\mathbf{J}$	Jacobian
$\mathbf{K}$, $\mathbf{A}$	structural, aerodynamic sti ness matrix
l_0	undeformed beam element length
l_w	wake length
L	lift, wing segment length
$M_{fs,t}$	folding, shearing, twisting actuation moment
M_a	aerodynamic moment
$\mathbf{n}$	normal vector
$\mathbf{p}$	degree-of-freedom vector
$\mathbf{p_\alpha}$	augmented degree-of-freedom vector
q	dynamic pressure
$\mathbf{R}$	residual vector
$\Re$	rotation matrix
$\mathbf{s}$	aerodynamic panel vector
$\mathbf{T}$	co-ordinate frame orientation
$\mathbf{u}$	global displacements
$\bar{u}$	local beam elongation
$\mathcal{U}$	strain energy
$\mathbf{V}_\infty$	undisturbed flow direction
$\mathbf{w_i}$	induced velocity
W	aircraft weight
x_c	collocation point
x_{qc}	quarter chord location
x_{tqc}	three-quarter chord location
x_{te}	trailing edge location
x_n, x_p	structural, aerodynamic nodes

Paper No. 3719. Manuscript received 12 May 2011,first revision received 26 June 2011, second revision received 2 September 2011, accepted 15 September 2011.
This paper is based on a presentation given at the 2010 RAeS 2nd Aircraft Structural Design Conference, London, UK.

Greek symbols

α	angle-of-attack
Γ	vortex strength per unit length
ε	strain vector
θ	global rotation
θ_f	folding angle
λ	load parameter
ξ	nondimensional co-ordinate
ρ	air density
ϕ_t	twisting angle
$\{\phi;\theta;\psi\}$	local nodal rotations
ψ_s	shearing angle

Subscript/Superscript

ℓ	local
g	global
m	master
r	rigid, root
s	slave
t	transpose

Co-ordinate frames

$T_b = [E_1\ E_2\ E_3]$ inertial frame
$T_g = [e_1^b\ e_2^b\ e_3^b]$ body-fixed frame
$T_r = [e_1\ e_2\ e_3]$ rigid element frame
$T_a = [e_l\ e_m\ e_\alpha]$ aerodynamic frame
$T_0 = [e_1^0\ e_2^0\ e_3^0]$ initial orientation frame
$Ti = [t_1^i\ t_2^i\ t_3^i]$ elastic frame

1.0 INTRODUCTION

Morphing of an aerospace structure is the radical change in shape of that structure. The aim of such large shape changes is to allow the aircraft to fly optimally in contradictory flight conditions. For instance a commercial airliner faces different flight conditions during its flight; flying slowly at high-lift during a holding manoeuvre, or flying at high speed during the cruise phase. A morphing outboard section of the wing could facilitate the aircraft to fly at the lowest possible drag for both flight conditions. In the broadest sense of the term, morphing aircraft have existed ever since the dawn of aviation, because in 1895, Otto Lilienthal, the father of modern aviation[1], developed his Vorflügelapparat, a glider which had an adaptive leading edge, and hence could actively change the camber line of the wing, as was stated during a presentation at the AIAA SDM conference 2010[2].

Co-ordinated research to morphing aircraft structures started in the last decade of the previous century by the Defense Advanced Research Projects Agency (DARPA), the Air Force Research Laboratory (AFRL), and NASA, and was extended to well into the first decade of this century[3-5]. The focus was mainly on application of smart materials to aircraft structures and development of multi-role combat aircraft. Ever since the start of the abovementioned initiative, the number of morphing wing research efforts has increased, and morphing is still under intensive research today[6]. Dedicated tools have been developed to analyse and design morphing aircraft as well[7,8,9]. Usually, these tools make use of commercially available analysis software packages and couple them loosely. This can cause the analysis to be slow, and it is more difficult to assess the structural, aerodynamic, and actuator effects, and their interaction. Therefore "there is a need for a fast and integrated analysis tool which can model arbitrary shape changes of a morphing wing." These are in fact the very words of Anna-Maria McGowan, program manager of the Morphing Program, during a presentation at a morphing aircraft workshop at IST, University of Lisbon, Portugal in December 2008[10].

This paper describes a nonlinear aeroelastic model which can calculate morphing deformations of arbitrary planform wings. The morphing deformations are discretised in three distinct morphing modes; wing folding, wing twisting, and wing shearing. With the combination of arbitrary combinations of these three mechanisms, and their distribution over the wing, virtually any morphed wing shape is attainable. The actuator energy consumption associated with the morphing deformations is evaluated as well, including aeroelastic effects. The aeroelastic model consists of a close coupling between a nonlinear beam model, using a corotational approach, and high-subsonic aerodynamics, modelled by the Weissinger method which is corrected using the Prandtl-Glauert correction. Using this aeroelastic analysis code, a morphing winglet, which is retrofitted to a regional airliner, is optimised to minimise the wing drag over an entire flight.

The paper is structured as follows. First the morphing wing problem formulation is given, which describes the morphing wing discretisation, and the relevant co-ordinate frames. Next, the nonlinear beam element model is described, followed by the aerodynamic model. The next section elucidates the way both the structural and aerodynamic model are coupled to obtain the aeroelastic solution. Then the mathematical details are given on how the morphing mechanisms are embedded into the aeroelastic solution procedure. This is followed by the results section showing the optimal configuration of the morphing winglet and compare its merits to a fixed winglet equipped wing. Finally an overview of the paper is given, and pertinent conclusions are drawn.

2.0 PROBLEM FORMULATION

The wing is divided into wing segments which have actuators between the two end-ribs of the segment, called intra-rib mechanisms, and actuators between two end-ribs of two adjacent wing segments, called inter-rib mechanisms. A detailed description of the morphing wing discretisation method can be found in De Breuker *et al* (2011)[11]. Arbitrary changes in wing shape are decomposed into three distinct deformation modes; (1) wing folding, (2) wing twisting, and (3) wing shearing, see Fig. 1. Twisting and shearing are intra-rib modes and folding is an inter-rib mode. A short description of these deformation modes follows:

1. Wing folding: the two end-ribs of two adjacent wing segments can rotate with respect to each other around an axis which is aligned the chord. This morphing concept is applied in the Lockheed Folding Wing Concept[12]. Also the Hyper-elliptic Cambered Span (HECS) aircraft is an example of fold morphing[13], as well as the work carried out at the University of Bristol on folding winglets[14].
2. Wing twisting: a relative rotation around the segment axis is prescribed. This morphing concept is investigated by many researchers[15-17].
3. Wing shearing: wing shearing is realised by moving the two end-ribs of a wing segment parallel to each other in the direction of the chord. In this fashion, the wing centre line shows a change in sweep. This concept has been investigated by multiple researchers[18-20].

Virtually any wing shape is attainable by an appropriate combination of prescribed folding, twisting, and shearing angles, while maintaining the continuity of the wing surface.

In order to analyse the morphing of wings. an appropriate model should include four important phenomena; large morphing deformations, aeroelasticity, structural straining during morphing, and the required actuator energy for the morphing manoeuvre. Aerodynamic loads change significantly due to the large deformations of the

https://doi.org/10.1017/S0001924000006461 Published online by Cambridge University Press

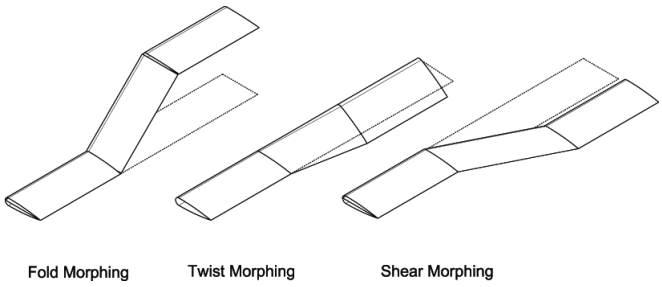

Figure 1. Wing morphing mechanisms
(dashed line shows original straight configuration).

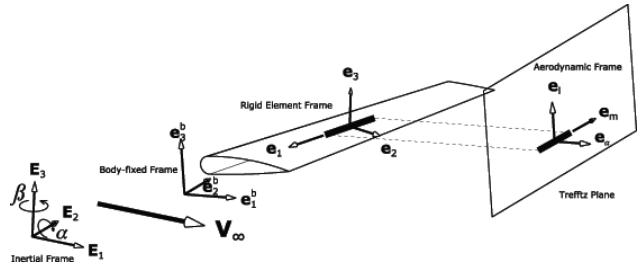

Figure 2. The four main co-ordinate frames of the morphing wing model.

morphing, hence aeroelasticity needs to be taken into account. Furthermore the aerodynamic loads and their change during the morphing affect actuator energy requirements and structural straining.

A corotational structural model is chosen which uses a linear beam element able to model composite wing cross-sections. The aerodynamics are modelled using Weissinger's method including the Prandtl-Glauert correction for high-subsonic flows. The structural and aerodynamic models are closely coupled, and the nonlinear aeroelastic equilibrium equations are solved using the Newton-Raphson iteration technique. Due to the nature of this model, four co-ordinate frames need to be constructed; (*i*) an element frame connected to each wing segment, (*ii*) a body-fixed coordinate frame in which all the wing segment deformations — sum of the elastic and rigid body deformations — are assembled, (*iii*) an aerodynamic frame in which the aerodynamic properties are calculated, and (*iv*) an inertial frame in which the morphing wing is free to 'fly'. In this frame, gravity is oriented in the negative $\mathbf{E}_3$-direction. The co-ordinate frames are shown in Fig. 2.

3.0 LIMITATIONS OF THE MODEL

The use of a low-fidelity static aeroelastic model is well-suited for fast analysis and for quick sizing a morphing wing, however, when interpreting the results, one should always take the assumptions of such a model into consideration when interpreting the results. Therefore a discussion on the limitations of the model is in order.

3.1 Dynamic aeroelasticity

This model consists of a static coupling between a nonlinear beam model and a Weissinger method aerodynamic model; therefore dynamic effects were not considered. This excludes important aeroelastic effects from the design considerations such as the effect of gust and flutter. In the case of gust load, and for preliminary design purposes for which the approach was designed, applying an appropriate load factor, e.g. taken from airworthiness manuals, to the static load cases is sufficient.

Using a static approach to model a morphing wing inherently assumes that the morphing is slow, i.e. no dynamic effects are to be expected from the morphing deformations. The morphing can be considered as a series of static snapshots. It is important, however, to check the dynamic aeroelastic stability of each of these snapshots to prevent phenomena such as flutter from happening during the slow morphing.

Some other dynamic aspects may not be as amenable to such a solution, for example making an assessment of the energy consumed by the morphing actuators. This is an inherent dynamic effect and it requires the modelling of the wing mass distribution. Nonetheless, the static results of the model should produce an order of magnitude estimate of morphing energy consumption.

3.2 Structural and aerodynamic model

The use of a beam model to model aeroelastic deformations limits the accuracy of the model, however, the prediction of deformations is suciently accurate for slender wings[21]. The model is not used for detailed sizing of the wing, and the aerodynamic model is naturally restricted to high-subsonic Mach numbers and for aspect ratios of no less than four. Transonic effects, shocks and separation, are not included. Since the model is trimmed to a given load factor, the model needs only to predict load distribution with sucient accuracy. The trimming analysis is done for a wing rather than for a total aircraft configuration. This affects the value of the trimmed angle-of-attack, but the trends predicted should be helpful to designers.

The weight of the wing is excluded from the static aeroelastic analysis. There is no inertia relief which means that the occurring root-bending-moment and deformations of the wing are overestimated. For conventional aircraft, which are considered in this paper, the weight of the wing is relatively small as compared to the total weight of the aircraft. Therefore, the lift on the wing in trimmed condition is significantly larger than the weight of the wing, because of which the effects of inertia relief on the static analysis of the morphing wing are expected to be minor.

The static aeroelastic model is applied to the design of a morphing wing excluding the presence of a fuselage and tail of the aircraft. The morphing wing is assumed to be clamped to a fixed point at its root. The implications of these assumptions is that the effects of flight dynamics are not included and that a trimmed condition of the wing means that the force equilibrium between the aerodynamic forces generated by the wing and the aircraft weight is ensured, but no overall aircraft moment equilibrium.

4.0 STRUCTURAL MODEL

The morphing wing is modelled using beam elements. The type of beam element used is a shear-flexible element which allows for the use of anisotropic materials. The structural model accounts for large displacements and rotations. The latter ones are complex due to their nonvectorial nature[22].

A corotational framework is used to account for the large deformations. Using the corotational approach, the elastic beam deformations are solved in the local element frame, which moves rigidly along with the element displacements and rotations[23-25] in a global frame. If the elastic deformations are small, one can suce with a linear local beam element. The use of the corotational framework makes the beam model geometrically nonlinear, which means that the beam stiffens when exhibited to large deformations. This causes the large deformations to become smaller when compared to linear analysis results.

The reason for using a shear flexible element stems from aeroelasticity, which requires the knowledge of the location of the shear centre of the cross-section. If the cross-sectional properties of the beam change, the shear centre would move as well. In case of a Timoshenko beam element, this is not an issue, since the coupling between shear and torsion of the beam, in case the stiffness matrix is calculated around a reference point di erent from the shear centre, is taken care of automatically.

https://doi.org/10.1017/S0001924000006461 Published online by Cambridge University Press

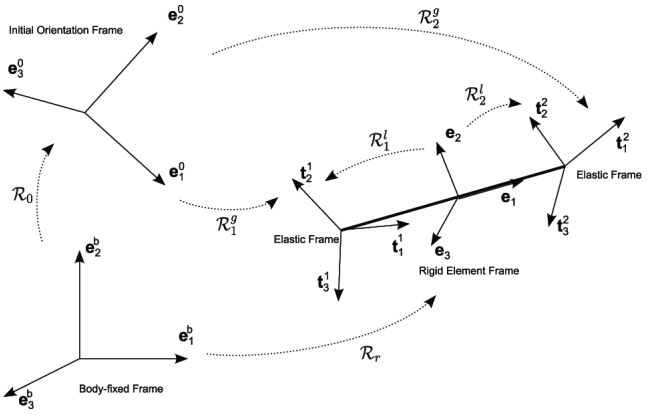

Figure 3. Relative position of the local and global co-ordinate frames.

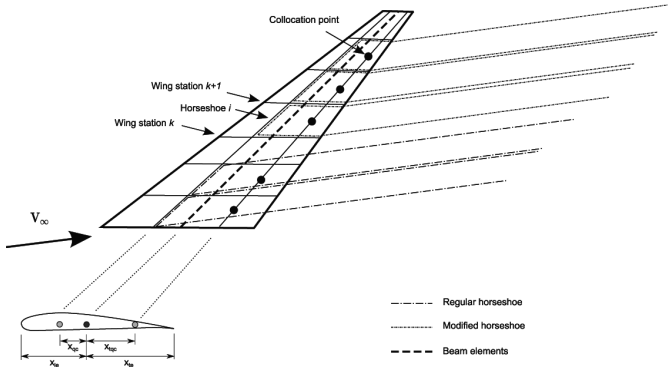

Figure 4. Aerodynamic discretisation of the wing and aerofoil.

4.1 Local element formulation

The local element is a linear shear-flexible Timoshenko element, which allows the use of anisotropic materials. The beam strain energy $\mathcal{U}$ is calculated to be[26],

$$\mathcal{U} = \frac{l_0}{2}\int_0^1 \boldsymbol{\varepsilon}^t \mathbf{C}\boldsymbol{\varepsilon} d\xi \qquad \ldots (1)$$

where $\boldsymbol{\varepsilon}$ is the strain vector, $\mathbf{C}$ is the constitutive matrix, which is interpolated linearly over the element, ξ is the nondimensional co-ordinate, and l_0 is the beam undeformed element length.

The local element equilibrium equation can be written as,

$$\mathbf{K}_\ell \mathbf{p}_\ell = \mathbf{f}_\ell \qquad \ldots (2)$$

where $\mathbf{K}_\ell$ is the local stiffness matrix. $\mathbf{f}_\ell$ is the local force vector associated with the local degrees-of-freedom (DOF) $\mathbf{p}_\ell$.

4.2 Corotational framework

The method which is used to link the force vector and stiffness matrix expressed in the local element frame to those expressed in the body-fixed frame, also referred to as global frame, is adopted from Battini and Pacoste[25]. For each beam element, the global DOF vectors looks like,

$$\mathbf{p} = \left\{ \mathbf{u}_1^t \ \boldsymbol{\theta}_1^t \ \mathbf{u}_2^t \ \boldsymbol{\theta}_2^t \right\}^t \qquad \ldots (3)$$

where vectors $\mathbf{u}$ are the global displacements and $\boldsymbol{\theta}$ are the pseudo-vectors of the global nodal rotations. The relative positions of the global and local co-ordinate frames are depicted in Fig. 3.

In this figure it is shown that there are in total five co-ordinate systems. Two of them are already known from Fig. 2, namely the body-fixed or global co-ordinate frame T_b, and the rigid element frame T_r. The other two are the element initial orientation frame T_0, which indicates the initial orientation of the element in the global co-ordinate frame, and the elastic beam node triads T_i which define the orientation of the local beam nodal cross-sections.

The relation between the global and local force vectors and sti ness matrices is defined by Battini[25] as,

$$\mathbf{f} = \mathbf{B}^t \mathbf{f}_\ell \qquad \ldots (4)$$

$$\mathbf{K} = \mathbf{B}^t \mathbf{K}_\ell \mathbf{B} + \frac{\partial \mathbf{B}}{\partial \mathbf{p}} : \mathbf{f}_{t\ell} \qquad \ldots (5)$$

where the colon indicates a contraction, and transformation matrix $\mathbf{B}$, which is an explicit function of $\mathbf{p}$, can be found in Battini and Pacoste[25]. Transformations of the displacements from the local to the global framework is a matter of redefining the nodal positions of the beam element in the other co-ordinate frame, and the relation between the global and local rotations is obtained by looking at the orientation of the nodal cross-sections in Fig. 3,

$$\mathfrak{R}_i^l = \mathbf{T}_r^t \mathfrak{R}_i^g \mathbf{T}_0 \qquad \ldots (6)$$

5.0 AERODYNAMIC MODEL

A high-subsonic flow of a slender high aspect ratio wing can be solved using theWeissinger[27] method to which a Prandtl-Glauert correction is applied[28]. The latter correction scales the chordwise co-ordinate with a factor $1/\sqrt{1-M^2}$, where M is the Mach number of the undisturbed flow. The vortex distribution over the wing is discretised into a number of horseshoe vortices. This type of vortex consists of a bound vortex, which is located on the quarter-chord line of the wing (x_{qc}), and trailing vortices, which extend downstream to infinity, hence forming a horseshoe.

To account for large angles-of-attack, the trailing vortices are split up into a part on the wing in the direction of the wing chord, and a part extending from the wing trailing edge in the direction of the free stream. This can be inspected in Fig 4.

In the special horseshoe case, adapted for large angles-of-attack, each horseshoe vortex consists of six points, two at infinity, two at the trailing edge (x_{te}), and two at the quarter-chord line. The panel co-ordinate points $\mathbf{x}_p$ of each horseshoe vortex are derived from the beam nodal locations $\mathbf{x}_n$ as follows,

$$\begin{cases} x_{p,1,i} = x_{n,k} + x_{te,k}\cdot c_k + l_w \cdot \{\mathrm{Cos}\alpha \ 0 \ \mathrm{Sin}\alpha\}^t, \\ x_{p,2,i} = x_{n,k} + x_{te,k}\cdot c_k, \\ x_{p,3,i} = x_{n,k} + x_{qc,k}\cdot c_k, \\ x_{p,4,i} = x_{n,k+1} + x_{qc,k+1}\cdot c_{k+1}, \\ x_{p,5,i} = x_{n,k+1} + x_{qc,k+1}\cdot c_{k+1}, \\ x_{p,6,i} = x_{n,k+1} + x_{qc,k+1}\cdot c_{k+1} + l_w \cdot \{\mathrm{Cos}\alpha \ 0 \ \mathrm{Sin}\alpha\}^t, \end{cases} \qquad \ldots (7)$$

where l_w is the length of the wing wake, α is the angle-of-attack, and $\mathbf{c}$ is the direction of the chord in the deformed configuration,

$$\mathbf{c} = \mathfrak{R}^g \mathbf{c}_0 \qquad \ldots (8)$$

where $\mathbf{c_0}$ is the undeformed initial chord direction and $\mathfrak{R}^g$ is shown in Fig. 3.

The unknown vortex distribution is solved using Weissinger's method by requiring the flow normal to the wing to be equal to zero. This requirement is fulfilled in the collocation point at the three quarter chord point (x_{tqc}), see Fig. 4. The positions of the collocation point x_c are calculated as,

https://doi.org/10.1017/S0001924000006461 Published online by Cambridge University Press

$$\begin{cases} x_{p,1,i} = x_{n,k} + x_{te,k} \cdot c_k + l_w \cdot \{\mathrm{Cos}\alpha\ 0\ \mathrm{Sin}\alpha\}^t, \\ x_{p,2,i} = x_{n,k} + x_{te,k} \cdot c_k, \end{cases} \quad \ldots (9)$$

The normal velocity in the collocation point of a horseshoe vortex consists of two parts; the induced velocity caused by the vortex distribution over the wing (the influence of vortex Γ_j on collocation point i is influence coecient a_{ij}), and the normal velocity component of the undisturbed flow velocity $\mathbf{V}_\infty$. Equating both yields the governing equation of the unknown vortex distribution,

$$a_{ij}\Gamma_j = -\mathbf{V}_\infty \cdot \mathbf{n}_i \quad \ldots (10)$$

where $\mathbf{n}_i$ is the normal vector of the ith horseshoe vector.

The solution of this equation results in the unknown vortex distribution over the wing span. This vortex distribution is a measure for the lift distribution. The lifting force on the ith aerodynamic panel is expressed, following the Kutta-Joukowski theorem[29,30], as,

$$L_i = \rho V \infty \Gamma_i \|\mathbf{s}\| \quad \ldots (11)$$

where ρ is the air density, and $\|\mathbf{s}\|$ is the length of the projection of the bound vortex of the quarter-chord line on the Trefftz plane[27,30,31].

The induced drag is calculated using a Trefftz plane analysis. This type of analysis basically derives the force in flow direction by looking at the momentum change over a control volume, containing the wing, which is closed by the Trefftz plane. The induced drag on aerodynamic panel i becomes,

$$D_{i,i} = -\frac{\rho}{2}\Gamma_i \mathbf{w}_{i,j} \cdot \mathbf{n}_i \|\mathbf{s}\| \quad \ldots (12)$$

where $\mathbf{w}_{i,i}$ is the induced velocity on panel i generated by all the trailing vortices of the wing.

Since Weissinger method is an inviscid aerodynamic theory, no viscous drag can be calculated directly. However this drag contribution is important because of which an estimate of the viscous drag coecient $C_{D,v}$ can be made, based on for instance aerodynamic results for NACA aerofoils[32], as,

$$C_{D,v} = C_1 + C_2 C_L^2 \quad \ldots (13)$$

where coefficients C_1 and C_2 are characteristic for a particular aerofoil, and C_L is the lift coefficient.

The aerodynamic moment M_a is is calculated as the multiplication of the normal component of the lifting force and the distance between the aerodynamic centre and the reference point in the cross-section around which the constitutive matrix is calculated,

$$M_{a,i} = x_{qc,i}\mathbf{n}_i^t \cdot \mathbf{e}_{l,i} L_i, \quad \ldots (14)$$

where e_l is the direction in which the lift acts, see Fig. 2.

The lift force, the total drag and aerodynamic moment are now used to calculate the aerodynamic force vector $\mathbf{f}_a$ by decomposing the scalar quantities derived above into their appropriate directions of the aerodynamic frame, which is shown in Fig. 2, and assigning them to the appropriate degrees-of-freedom in the vector. Differentiating each individual component of vector $\mathbf{f}_a$ with respect to the global elements of degree-of-freedom vector $\mathbf{p}$ yields the aerodynamic stiffness matrix $\mathbf{A}$.

6.0 STATIC AEROELASTIC SOLUTION

The aeroelastic solution is obtained by equilibrating the internal forces, $\mathbf{f}$, and the external aerodynamic forces $\mathbf{f}_a$. The following equation is then to be solved,

$$\mathbf{f}(\mathbf{p}) = \mathbf{f}_a(\mathbf{p}, q, \alpha); \quad \ldots (15)$$

where q is the dynamic pressure. In case the trimming condition is enforced, an additional equilibrium equation is added to the system, namely that the total vertical aerodynamic force is equal to the aircraft weight, yielding the following system to be solved,

$$\begin{cases} \mathrm{f}(\mathbf{p}) = \mathrm{f}_a(\mathbf{p}, q, \alpha) \\ R^{r,t} \cdot e_l^r + W = 0 \end{cases} \quad \ldots (16)$$

where W is the total weight of the aircraft, and $\mathbf{R}^r$ are the reaction forces at the root of the wing.

Vector $\mathbf{e}_l^r$ is the direction of the lift force at the root of the wing, expressed as,

$$\mathbf{e}_l^r = \{-\mathrm{Sin}\alpha\ 0\ \mathrm{Cos}\alpha\}^t \quad \ldots (17)$$

In case trimming of the aircraft is required, the angle-of-attack becomes a degree-of-freedom as well, since it is not known *a priori*. Therefore the DOF vector $\mathbf{p}$ is augmented to $\mathbf{p}_\alpha = \{\boldsymbol{p}^t\ \boldsymbol{\alpha}\}^t$.

In order to solve the nonlinear aeroelastic system, the Newton-Raphson method is employed[33]. This is a root-finding algorithm based on Taylor series expansions. Since the system is highly nonlinear, it is not possible to solve the equilibrium equation at a given flight speed in one step. Therefore the intended flight speed is divided in steps, controlled by the parameter λ ranging from 0 to 1. Every time λ is advanced to the next velocity level, a converged set of degrees-of-freedom $\mathbf{p}$ needs to be found. A prediction of the aeroelastic deformation $\mathbf{p}_\alpha$ for increasing λ can be obtained by expanding Equation (16) around an equilibrium point $\mathbf{p}_{\alpha,0}$,

$$\begin{bmatrix} \mathbf{J} & -f_\alpha \\ \mathbf{J}^r \mathbf{e}_l^r & R^{t,r}\frac{\mathrm{d}\mathbf{e}_l^r}{\mathrm{d}\alpha} + f_\alpha^{t,r}\mathbf{e}_l^r \end{bmatrix} \partial \mathbf{p}_\alpha = -\begin{Bmatrix} \mathbf{R}_0 \\ W + \mathbf{R}_0^t \mathbf{e}_l^r \end{Bmatrix} - \begin{Bmatrix} \frac{\partial \mathbf{R}}{\partial \lambda} \\ \frac{\partial \mathbf{R}^{t,r}}{\partial \lambda}\mathbf{e}_\lambda^\rho \end{Bmatrix} \partial\lambda, \quad \ldots (18)$$

where $J = \frac{\partial \mathbf{R}}{\partial \mathbf{p}}, f_\alpha = \frac{\partial \mathbf{f}_a}{\partial \alpha}$, and $\mathbf{R}_0$ is the residual force vector evaluated at $\mathbf{p}_{\alpha,0}$. The variation of p is indicated with a δ. The prediction of the aeroelastic deformation is now,

$$\mathbf{p}_\alpha = \mathbf{p}_{\alpha,0} + \delta \mathbf{p}_\alpha \quad \ldots (19)$$

This prediction now needs to be corrected following a similar strategy as described above, but while keeping λ constant. The above derivation also holds for non-trimmed configurations, but in that case, all derivatives with respect to α are equal to zero, and there is no requirement that the wing lift should be equal to the aircraft weight.

7.0 MORPHING MECHANISMS

The morphing deformations of the wing are obtained by using three distinct morphing modes, as described in Section 2. The implementation of each of these modes into the aeroelastic solution procedure, described in Section 6, is given in detail in this section.

7.1 Fold morphing

The morphing wing is modelled as a beam. At the locations where the wing is allowed to fold, each node is replaced by two colocated nodes, which transfer the structural displacements, but not the rotations. The rotational stiffness is provided by springs, which mimic the folding actuator stiffness. One of the nodes' rotations are dependent on the rotations of the other colocated node. The dependent node is called the slave node (referenced using a superscript s), and the independent one is the master node (referenced using a superscript m).

In order to ensure continuity of the wing surface, the relative folding rotation θ_f between two wing segments must take place around the rib axis $\mathbf{c}$ connecting those two wing elements. Vector $\mathbf{c}$ rotates along with the aeroelastic deformations, so from a mathematical point-of-view it is more convenient to express the relative rotation θ_f around the

https://doi.org/10.1017/S0001924000006461 Published online by Cambridge University Press

undeformed chord c_0, and apply the aeroelastic deformation afterwards. A rotation $\boldsymbol{\theta}_f$ around c_0 can be written as the rotation matrix $\mathfrak{R}_f$ or in pseudo-vectorial format as $\boldsymbol{\theta}_f$. This results in the following relation between the slave and the master rotations at the node where the folding takes place,

$$\mathfrak{R}^{t,m}\mathfrak{R}^{s} = \mathfrak{R}_{\mathbf{f}} \quad \ldots (20)$$

where $\mathfrak{R}^{\mathbf{m}}$ is the master node rotation matrix, $\mathfrak{R}^{\mathbf{s}}$ is the slave node rotation matrix. The left-handside of Equation (20) can be denoted with $\mathfrak{R}_{\mathbf{x}}$, which yields the following equation in pseudo vectorial format for a particular rotation level λ,

$$\theta_x - \lambda\,\theta_f = 0 \quad \ldots (21)$$

Equation (21) can be added to the aeroelastic equilibrium equations 15 as a constraint equation for each folding station. The corresponding folding moment $\boldsymbol{M}_f$ is obtained from the Newton-Raphson analysis and are essentially the Lagrange multipliers associated with the constraint Equation (21). The energy consumed by the actuators to effectuate the folding action is expressed as,

$$E_f = \int_0^t \mathbf{M}_f^t \cdot \theta_f \mathrm{d}\lambda. \quad \ldots (22)$$

7.2 Shear morphing

Shear morphing makes the wing shear in its own plane. The objective is to change the sweep angle distribution over the wing span. A shear angle can be imposed on every beam element individually, with the important boundary condition that the shearing should not result in an elastic rotation of the beam element cross-sections. Therefore the following relation holds,

$$\mathfrak{R}^{g}_{i,el}\mathbf{T}_r\mathfrak{R}^{r,t}_{s} = \mathfrak{R}^{g}_{i}\mathbf{T}_0 \quad \ldots (23)$$

where superscript *el* indicates the fact that the rotations are only elastic, and $\mathfrak{R}^{r}_{s}$ is the rotation matrix representing the shear around the normal axis e_3 in the rigid rotation frame $\boldsymbol{T}_r$ with a shear angle ψ_s. This equation shows that the elastic rotations, expressed in the global frame, are imposed on the rigid element frame $\boldsymbol{T}_r$, which is rotated back by the shearin g rotation $\mathfrak{R}_{\mathbf{s}}$ should be equal to the total rotation imposed on the initial element orientation frame $\boldsymbol{T}_0$. Therefore the shearing as such does not cause elastic rotation of the element nodes. Equation 23 can be rearranged as,

$$\mathfrak{R}^{g}_{i,el}\mathbf{T}_r = \mathfrak{R}^{g}_{i}\mathbf{T}_0\mathfrak{R}^{r}_{s} \quad \ldots (24)$$

Premultiplying Equation (24) with $\boldsymbol{T}_r^t$ yields the expression for the elastic rotations in the rigid beam element frame,

$$\mathfrak{R}^{l}_{i} = \mathbf{T}^t_r\mathfrak{R}^{g}_{i,el}\mathbf{T}_r = \mathbf{T}^t_r\mathfrak{R}^{g}_{i}\mathbf{T}_0\mathfrak{R}^{r}_{s} \quad \ldots (25)$$

If this relation is compared to Equation 6, it becomes clear that imposing shear morphing on a beam element means that the shearing can be imposed on the element in its original orientation state before applying the loads onto the element. Note that initially the rotation matrix $\mathfrak{R}_{\mathbf{s}}$ was defined in the rigid beam element frame, hence the superscript *r*, but that this matrix does not change when defined in the initial beam orientation frame $\boldsymbol{T}_0$, so therefore superscript *r* can be removed from $\mathfrak{R}_{\mathbf{s}}$.

The associated shearing moment is obtained by differentiating the strain energy in the element by the shearing angle ψ_s,

$$\begin{aligned} M_s &= \frac{\partial}{\partial \Psi_s}\left(\frac{1}{2}\mathbf{p}^t_\ell \mathbf{K}_\ell \mathbf{p}_\ell\right) \\ &= \mathbf{f}^t_\ell \frac{\partial \mathbf{p}_\ell}{\partial \Psi_s} \end{aligned} \quad \ldots (26)$$

An additional moment requirement can come from the fact that skin spanning the wing segment shears and possesses a shear stiffness *GA*. In this case, a linear relation between the shearing moment and the shearing angle ψ_s is assumed, which leads to the updated equation for the required shearing moment,

$$M_s = \mathbf{f}^t_\ell \frac{\partial \mathbf{p}_\ell}{\partial \Psi_s} + GA\Psi_s \quad \ldots (27)$$

The energy E_s associated with the shearing deformation becomes,

$$E_s = \int_0^t M_s \Psi_s \mathrm{d}\lambda. \quad \ldots (28)$$

7.3 Twist morphing

A morphing twist angle ϕ_t is obtained by imposing this twisting differential rotation on the local element rotations around the element $\boldsymbol{e}_1$ axis. This is done in the following fashion,

$$\mathbf{p}_\ell = \left\{\bar{u}\;\phi_1\;\theta_1\;\psi_1\;\phi_2\;\theta_2\;\psi_2\right\}^t \left\{0\;-\tfrac{1}{2}\phi_t\;0\;0\;\tfrac{1}{2}\phi_t\;0\;0\right\}^t \quad \ldots (29)$$

where $\bar{u}$ is the beam axial elongation and ϕ, θ and ψ are the local nodal rotations. This approach makes sure that the beam element needs to twist around its own axis, which results in a set of rotations at both nodes of which the difference is exactly the imposed twisting angle. These rotations are obtained without straining the element, so in the absence of external loads, this twisting angle is obtained in a force-free way. The associated twisting moment is obtained by di erentiating the strain energy in the element by the twisting angle ϕ_t,

$$\begin{aligned} M_t &= \tfrac{\partial}{\partial \phi_t}\left(\tfrac{1}{2}\mathbf{p}^t_\ell \mathbf{K}_\ell \mathbf{p}_\ell\right), \\ &= \mathbf{f}^t_\ell \tfrac{\partial \mathbf{p}_\ell}{\partial \phi_t}. \end{aligned} \quad \ldots (30)$$

An additional moment requirement can come from the fact that the wing segment is restrained to warp. In this case, a linear relation between the twisting moment and the twisting angle ϕ_t is assumed, which leads to the updated equation for the required twisting moment,

$$M_t = \mathbf{f}^t_\ell \frac{\partial \mathbf{p}_\ell}{\partial \phi_t} + GJ\phi_t \quad \ldots (31)$$

where *GJ* is only nonzero if a warping restraint is present[17]. The twisting energy E_t associated with the morphing manoeuvre becomes the integral of the moment, which changes with changing twisting angle, over the twisting angle range,

$$E_t = \int_0^t M_t \phi_t \mathrm{d}\lambda. \quad \ldots (32)$$

Table 1
Aeroelastic validation case wing properties

Half span [m]	16
Chord [m]	1
Elastic axis	50% chord
Bending rigidity [Nm²]	2×10^4
Torsional rigidity [Nm²]	1×10^4
Bending rigidity (edgewise) [Nm²]	5×10^6

Table 2
Aeroelastic validation case flight conditions

Altitude [km]	20
Air density [kg m³]	0·0889
Flight speed [ms]	25
Angle-of-attack [deg]	2

https://doi.org/10.1017/S0001924000006461 Published online by Cambridge University Press

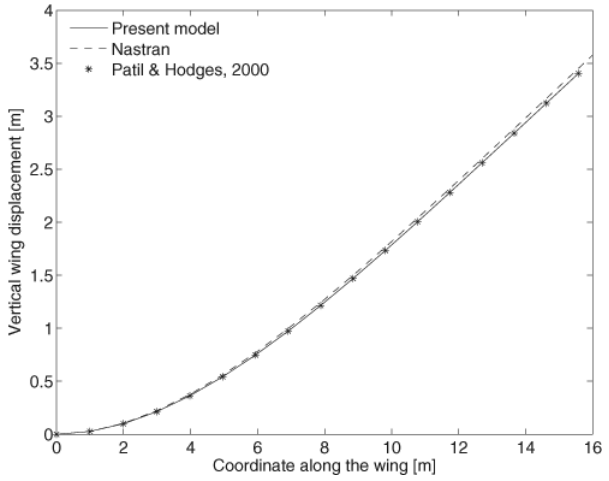

(a) Vertical wing displacement

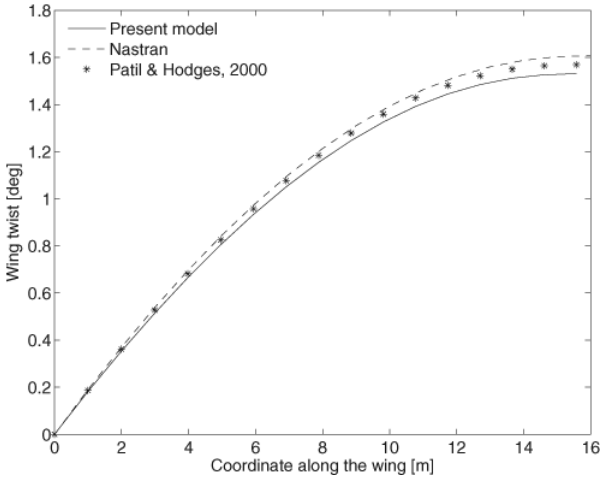

(b) Wing twist

Figure 5. Straight wing validation.

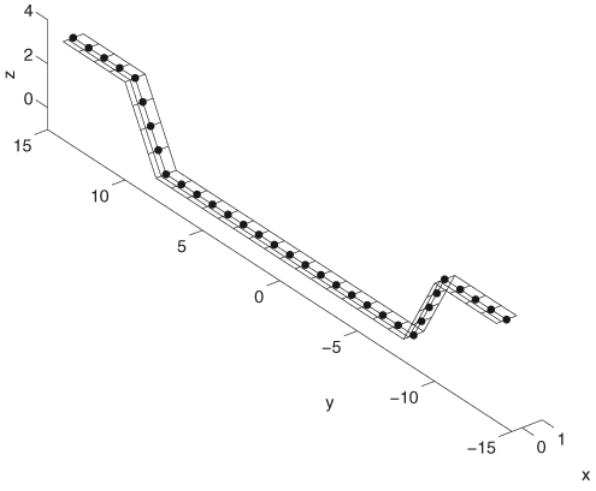

(a) Folded configuration

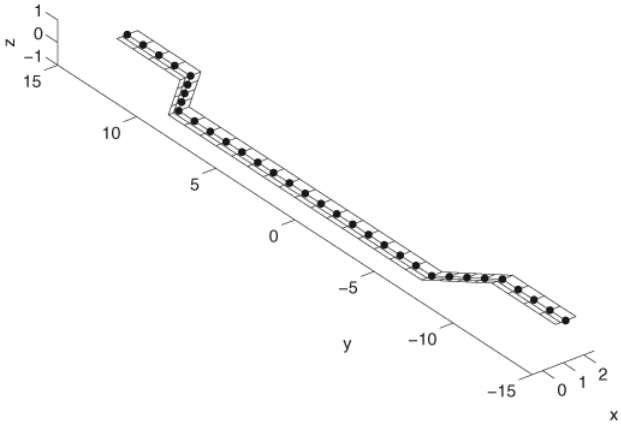

(b) Sheared configuration

Figure 6. Morphed configurations for the aeroelastic validation.

8.0 AEROELASTIC MORPHING MODEL VALIDATION

As a validation case, the aeroelastic deformations of a highly flexible wing are used. The wing is taken from Patil and Hodges[21] and is designed for a high-altitude long-endurance (HALE) aircraft. This model from Patil and Hodges[21] includes geometrical nonlinearities, which stiffens the wing at large deflections, and hence limits the displacements. Its geometric and stiffness properties are listed in Table 1. The flight conditions of the aeroelastic test case are listed in Table 2. The vertical wing displacement and wing twist of the straight wing configuration, as described in Patil and Hodges[21], are compared to the results of the present aeroelastic model.

Moreover, a Nastran aeroelastic model is developed with the same properties as in Tables 1 and 2 to compare to the results of the present model and the results of Patil and Hodges[21]. Reason for this additional validation of the Nastran model is to compare Nastran results to aeroelastic results of the present model for morphed configurations. The vertical displacement and wing twist results are shown in Figs 5(a) and 5(b), respectively. It can be observed that good correspondence exists between all three results.

For the morphing deformation validation, fold and shear morphing are compared. There is no need to validate the deformation field of a twisted wing, since the straight wing configuration[21] at the given angle-of-attack can be considered as a twisted wing with a constant twist angle. The undeformed morphed configurations are shown in Figs 6(a) and 6(b). The wings have the same material and geometric properties as the straight wing, only for the flight conditions, the sheared and twisted wing have a flight speed of 25ms^{-1}, as the straight wing, but the folded wing flies at 10ms^{-1} because 25ms^{-1} would lead to nonlinear deformations.

The results for vertical wing displacement and wing twist are shown below and show good correspondence. Only the tip twist of the folded configuration shows a difference of 10%, but that is because the twist angle as such is very small (one order of magnitude lower that the other morphed results), which makes the comparison prone to larger discrepancies, but this has clearly no influence on the deformation results.

The validation of the actuation moments is done using the same wing as is used for the aeroelastic displacement and rotation validation.

For the validation of the folding moment, the actuation moment required to prevent the tip wing element from rotation with respect to its neighbour is looked at. The wing is loaded with a static tip

https://doi.org/10.1017/S0001924000006461 Published online by Cambridge University Press

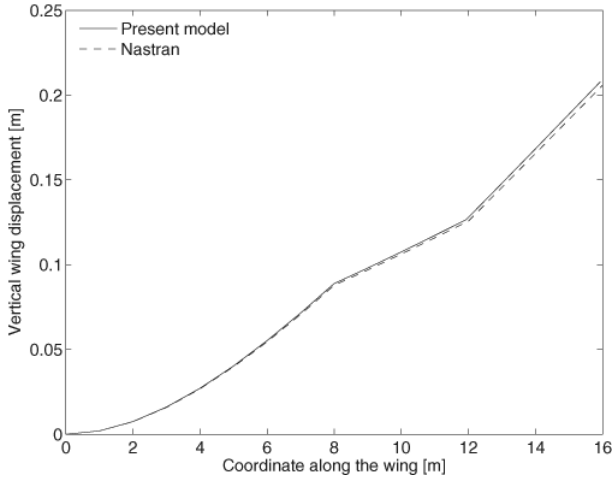

(a) Vertical wing displacement

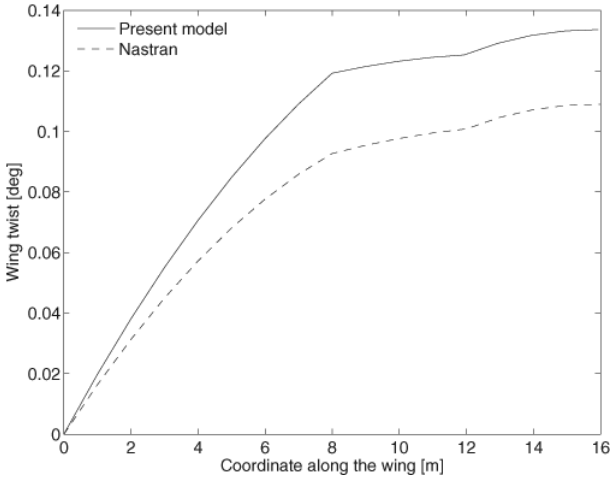

(b) Wing twist

Figure 7. Folded wing validation.

Table 3
ATR42-300 wing data

Wing span [m]	24·60
Wing surface area [m^2]	54·70
Aspect ratio [-]	11·10
Root chord [m]	2·57
Tip chord [m]	1·45

force F_z in a direction perpendicular to the wing surface, and with a magnitude of 500N. This shear force leads to a tip deflection which is 76% of the wing semi-span. The folding moment is compared to the following analytical expression,

$$M_f = F_z\,(L - \Delta y) \quad \ldots (33)$$

In this equation, L is the length of the wing segment, and Δy is the di erence in spanwise displacement of the begin and end node of the tip wing segment. The comparison is plotted in Fig. 9 and good correspondence can be observed.

For the validation of the shear moment, the required moment to restrain the tip wing element from shearing is investigated. The wing is loaded with a tip shear force in chord direction with a magnitude of 10^5N. This leads to a deflection which is 72% of the wing semi-span. Obviously this is a nonlinear deflection. The required actuation moment is compared to an analytical expression, which expresses the required moment as follows,

$$M_s = F_x\,(\mathrm{L} - \Delta y) \quad \ldots (34)$$

In this equation, F_x is the applied shear force. The comparison can be found in Fig. 10, and as can be seen, the correspondence is excellent.

For the validation of the twisting moment, a restraining twisting moment is looked at. The external twisting moment is applied at the tip of the wing which is also used for the aeroelastic displacement and rotation validation. The last wing segment is prevented from twisting under this loading by applying an actuation twisting moment. The external twisting moment is generated by a vertical force F_z of 2,500N which is applied at the quarter chord line of the wing and which acts perpendicular to the wing surface. This force leads to a tip twist of 0·75rad. The actuation twisting moment is calculated analytically as,

$$M_t = F_z\,\mathrm{Cos}\phi\;0{\cdot}25c \quad \ldots (35)$$

The comparison between the calculated moment and the analytical expression is shown in Fig. 11 and very good correspondence can be observed.

9.0 RESULTS

In this section, results are presented for a morphing winglet which is retrofitted to an existing regional airliner, to be more specific the ATR42-300. The properties of the ATR42-300 wing are listed in Table 3.

The discretised wing model can be viewed in Fig. 12 for both the case of the ATR42-300 wing without and with a winglet. Figure 12(b) is identical to Fig. 12(a) with the sole exception that two beam elements are attached to the wing tips of the original ATR42-300 wing which are a structural model for the winglet. Initially, the winglet is unfolded, unswept, and untwisted. The root chord of the winglet is equal to the tip chord of the wing, the winglet length is 1·5m, and the taper ratio of the winglet is 0·5. Figure 12 shows the aerodynamic and structural discretisation used for the optimisation cases. The boxes are the aerodynamic panels on which the horseshoe vortices are defined, and the black dots indicate the location of the structural nodes. The lines connecting those nodes are the beam elements. The continuous black line which is located in front of the beam elements is the quarter chord line of the wing where the bound vortex of the horseshoe vortices is located.

9.1 Regional airliner mission

The morphing winglet is optimised for a flight with a length of approximately 800km, which is divided into four parts; climb, cruise, descent, and a holding pattern. Along this path, the altitude, equivalent airspeed, and mass of the aircraft change continuously. The flight path itself is discretised into distinct flight points at which one single value for the flight speed, altitude, and aircraft mass is defined. Furthermore each flight point has a never exceed speed, or dive speed. The values of the flight data is shown in Fig. 13. The black crosses indicate the flight points.

The drag of the original ATR42-300 wing along this flight path at cruise speed is the reference value which the morphing winglet should decrease. The drag variation along the flight is shown in Fig. 14.

9.2 Optimisation formulation

The morphing winglet is optimised for two types of objective functions. The first one is to minimise the drag at each individual

https://doi.org/10.1017/S0001924000006461 Published online by Cambridge University Press

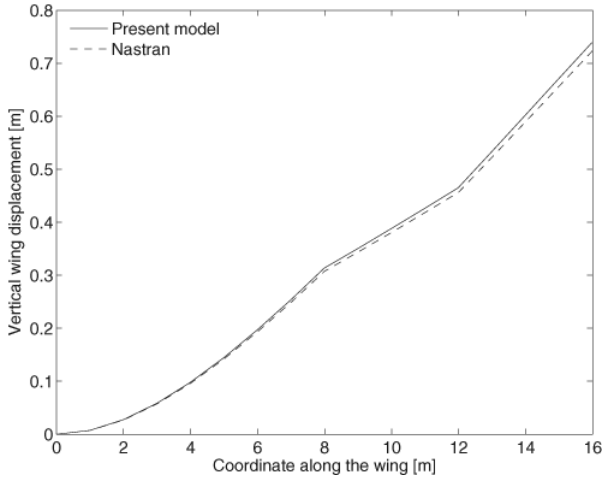

(a) Vertical wing displacement

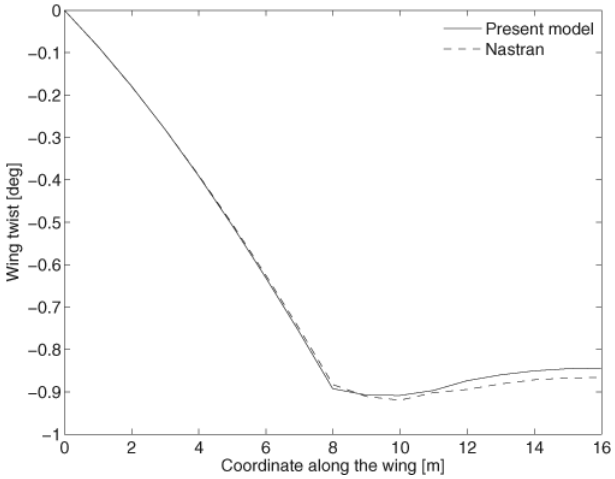

(b) Wing twist

Figure 8. Sheared wing validation.

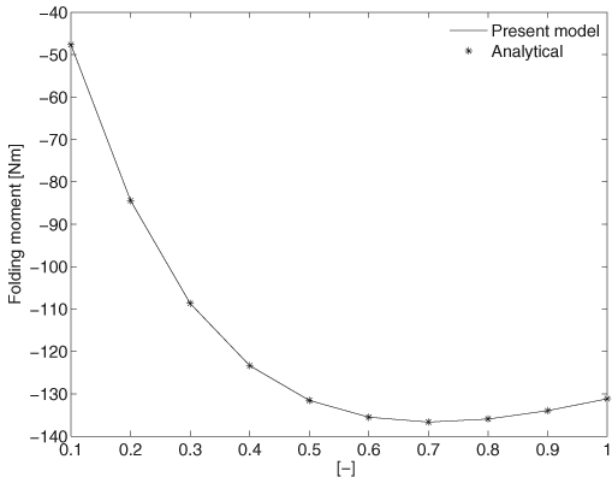

Figure 9. Folding moment validation.

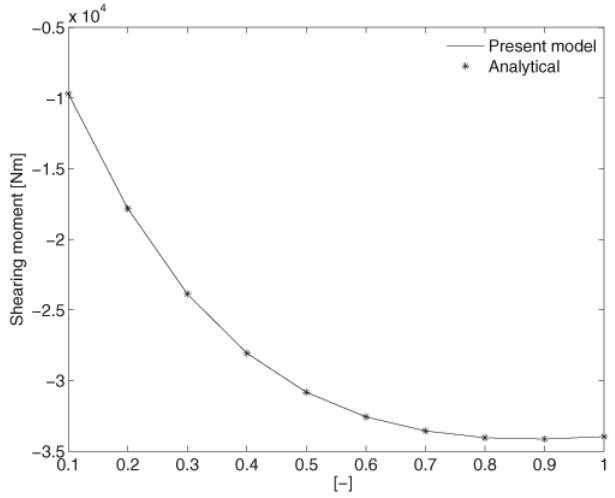

Figure 10. Shear moment validation.

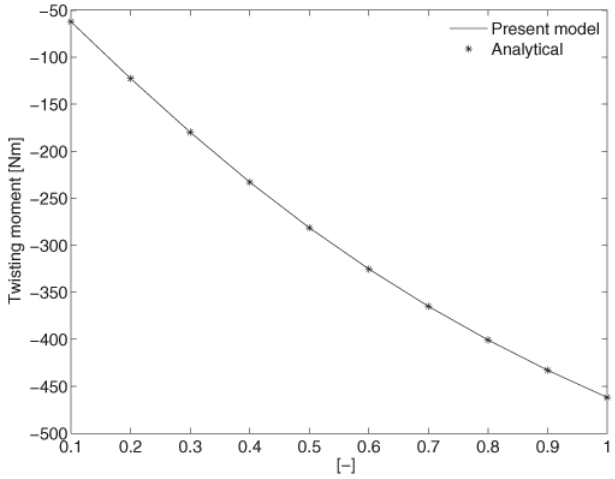

Figure 11. Twist moment validation.

flight point along the flight. This leads to a winglet which changes shape from one flight point to the other. The second objective is to optimise a winglet which minimises the total consumed energy of the aircraft wing over the flight. The energy consumption can be simplified to the integration of the wing drag over the flight path. This leads to a winglet which is fixed in one optimal configuration, and which is used as a comparison to the morphing winglet. Another comparison case is a winglet which is optimised to minimise the drag at the first flight point of the cruise flight. This yields three di erent winglet configurations which performance can be compared to the original ATR42-300 wing.

There are two nonlinear constraints associated with the optimisation problem. The first one is of aerodynamic origin. If the optimiser is leading the design into the direction of large morphing angles, it might be so that local stall occurs at specific parts of the wing. Therefore the local lift coefficient at each aerodynamic panel of the wing, including winglet, should remain between –1 and 1. The second constraint is of structural origin. Since the winglet under investigation is a retrofitted winglet, it is to be mounted onto an existing aircraft. In order not to compromise the structural integrity of the original wing structure, the increase in root bending moment (RBM) due to the retrofitted winglet should not exceed 2·5% at dive speed and at a load factor of 2·5. The increase in root bending moment of 2·5% stems from literature, where it was found that the allowed increase in RBM due to retrofitted winglets is between 1·4%[34] and 4·5%[35].

The design variables of the optimisation problem are the folding angle, shear angle, and twist angle of one of the two winglets. The

https://doi.org/10.1017/S0001924000006461 Published online by Cambridge University Press

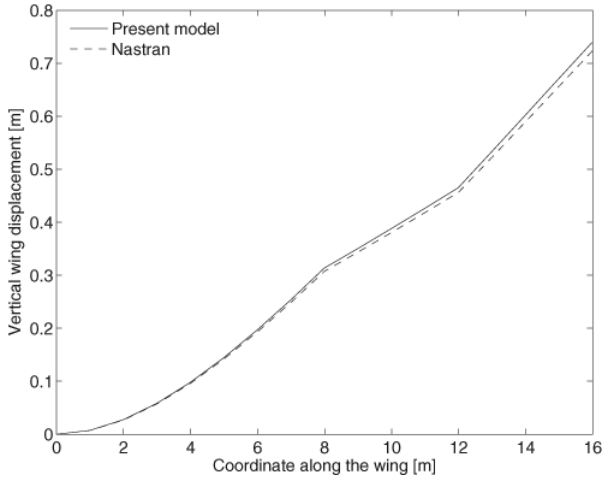

(a) Original ATR42-300 wing

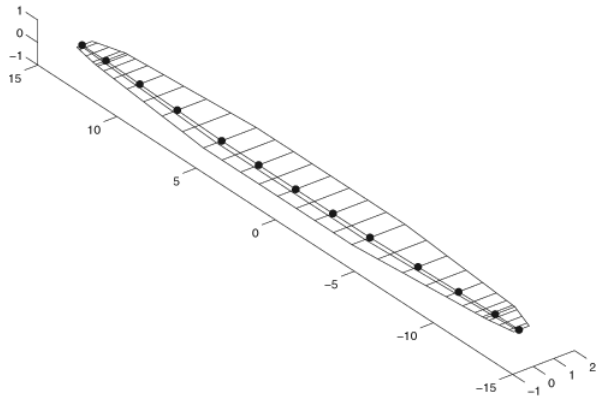

(b) ATR42-300 wing with winglet

Figure 12. ATR42-300 wing models.

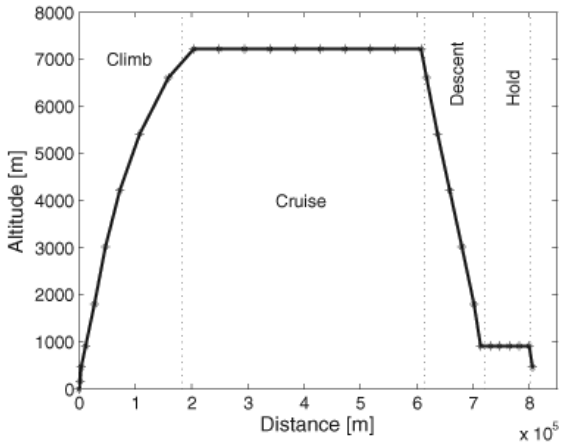

(a) Flight altitude

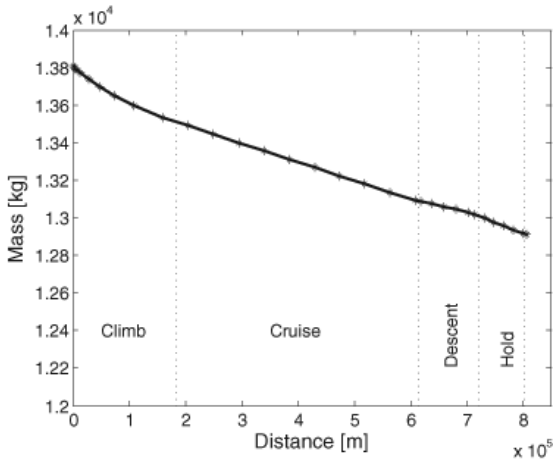

(b) Aircraft mass

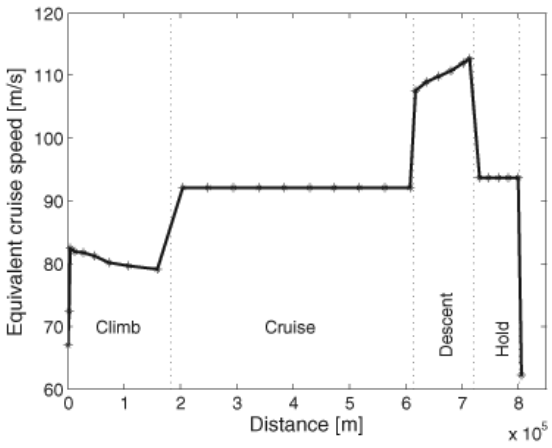

(c) Cruise speed

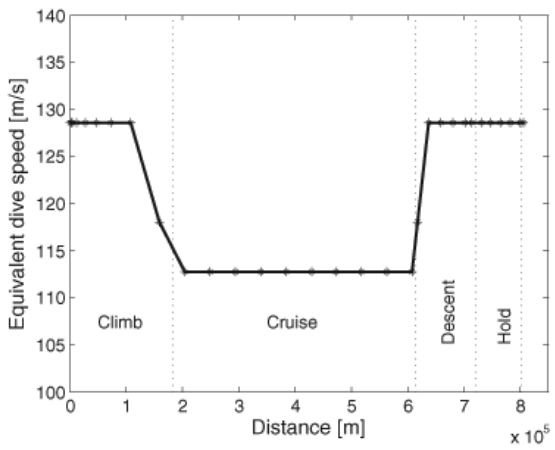

(d) Dive speed

Figure 13. ATR42-300 flight data.

other winglet is the mirrored version of the winglet which shape is defined by the design variables. The bounds on the design variables are listed in Table 4.

The optimisation technique used for the morphing winglet problem is nonlinear gradient based optimisation. A gradient-based method which is well-suited for nonlinear structural minimisation problems with nonlinear inequality constraints is the method of moving asymptotes (MMA)[36]. In this method, the nonlinear optimi-

https://doi.org/10.1017/S0001924000006461 Published online by Cambridge University Press

Table 4
Bounds on the design variables

Lower bound [deg]	Design variable	Upper bound [deg]
–90	Fold angle	90
–60	Shear angle	60
–57	Twist angle	57

Table 5
Consumed energy results for the three winglet cases

Wing case	Energy consumption [Nm]	Relative wrt original
Original	$4{\cdot}96 \times 10^9$	-
Morphing winglet	$4{\cdot}53 \times 10^9$	–3·5%
Fixed winglet cruise	$4{\cdot}62 \times 10^9$	–1·6%
Fixed winglet flight	$4{\cdot}62 \times 10^9$	–1·6%

sation is carried out by iteratively solving a convex approximation of the nonlinear objective function and inequality constraints. Since in aeroelastic optimisation problems, one is often confronted with non-smooth response surfaces with multiple extrema, the updated version of MMA, the globally convergent MMA (GCMMA)[37] is chosen in this paper. Since a gradient-based method is used, also the sensitivities of the objective function and potential constraint(s) with respect to the design variables are needed.

9.3 Morphing winglet optimisation results

The results for the three winglet cases (morphing winglet, fixed winglet optimised for the first flight point of cruise, and a fixed winglet optimised to minimise the consumed energy over the entire flight) are expressed as the drag reduction with respect to the original wing. The results are shown in Fig. 15. In this figure, the line of zero drag reduction is highlighted using a thick dashed line in order to indicate where the winglet is outperforming the original wing. This figure shows clearly that the morphing winglet outperforms the fixed winglets. The two fixed winglets which are optimised with two different strategies do not di er significantly in terms of drag reduction performance.

In order to compare the performances quantitatively, the consumed energy in terms of integration of drag over the flight, of the three winglet cases is compared to the consumed energy of the original aircraft. This is done in Table 5. Table 5 shows that the morphing winglet can reduce the energy consumption over an entire flight with 3·5%, which is more than two times as much as the energy saving of a fixed winglet.

One of the explanations can be found by looking at the moment constraint over the entire flight for the three winglet cases in Fig 16. In this figure, the bound is indicated with a thick dashed line. Furthermore it can be seen that the root bending moment for both fixed winglets is at its maximum at the flight point where the aircraft weight is the largest. Then it decreases gradually over the flight. The morphing winglet keeps the root bending moment close to the allowed value for a large part of the flight, except during the descent phase. Because of this, the morphing winglet can always manoeuvre itself into more favourable configurations, hence improving the drag performance of the wing further.

Now the change of the morphing angles over the flight is discussed. The fold angle starts from a negative value, which means that the winglet is folded down. This is an interesting result, since most of the winglets on commercial aircraft are folded upwards. The main reason for doing this is ground clearance during landing and/or take-off. There are many examples of winglets with a negative folding angle, such as the McDonnell Douglas MD-11 aircraft, the Gulfstream Peregrine, or the hyper-elliptic cambered span (HECS) wing[38]. The reason for folding down is that the induced drag is reduced by increasing the aspect ratio of the wing while reducing the increased root bending moment due to the winglet. The aerodynamic

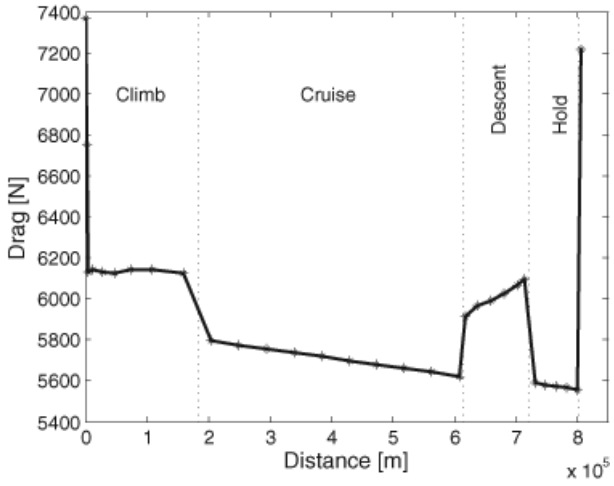

Figure 14. Drag change during flight.

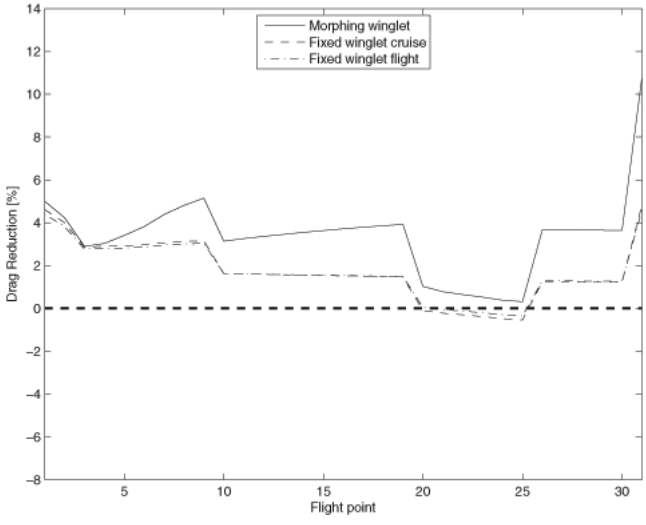

Figure 15. Relative drag for the three optimised winglet cases.

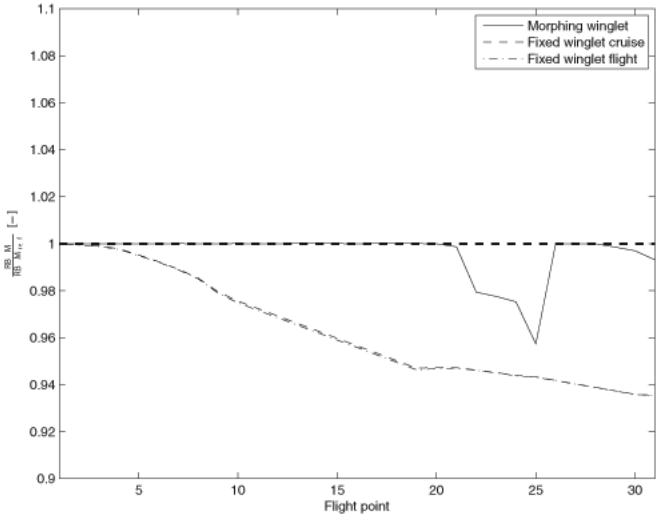

Figure 16. Moment constraint for the three optimised winglet cases.

https://doi.org/10.1017/S0001924000006461 Published online by Cambridge University Press

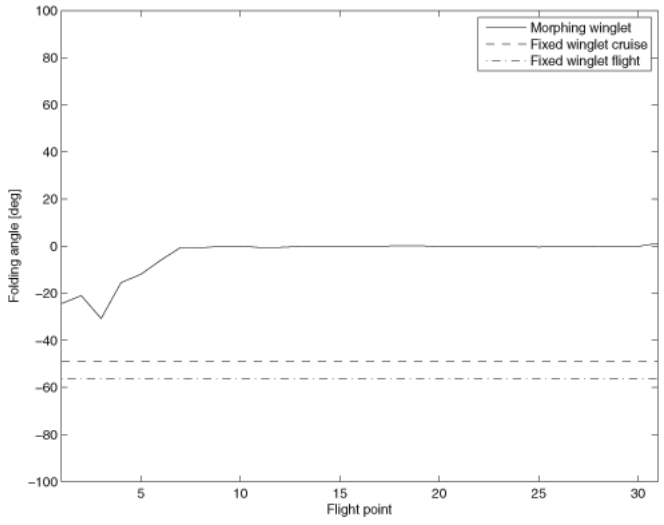

Figure 17. Change in folding angle of the morphing winglet.

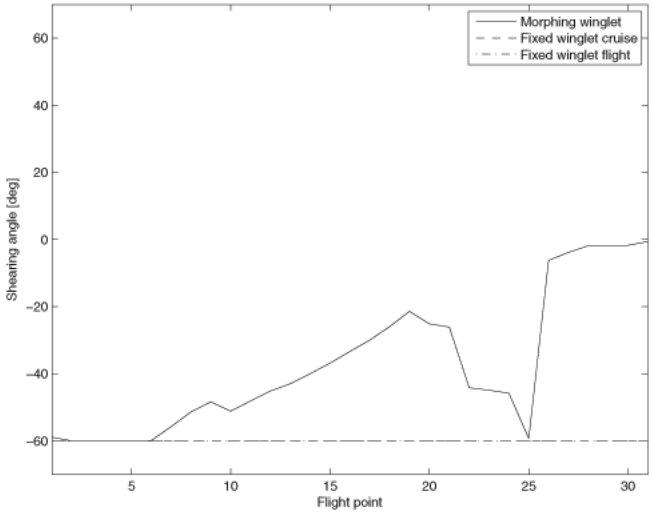

Figure 18. Change in shearing angle of the morphing winglet.

force on the winglet causes a counter-acting moment contrary to the moment due to the lift on the wing. The beneficial direction of lifting force on the winglet is caused by a washout angle of the winglet, which is shown in Fig. 19 and will be discussed below. The winglet folding angle reduces when the flight progresses because the weight of the aircraft reduces, and hence the loading on the wing. Therefore the winglet starts to extend to almost zero degrees folding angle to maximise the wing aspect ratio and hence reduce the induced drag. The change in folding angle is shown in Fig. 17. The constant folding angles of the fixed winglets are between 45 and 60 degrees downwards.

The winglet shears downstream to its bound of 60 degrees. The reason for this is that the addition of a winglet to the original wing causes the viscous drag to increase. In order to remove as much wing surface area as possible, the winglet shears downstream. And, as is also the case for the change in folding angle of the morphing winglet, the shear angle reduces when the wing loading reduces in order to maximise the wing aspect ratio to reduce the induced drag. The change in shear angle can be inspected in Fig. 18. The fixed winglets both have a shearing angle of 60 degrees downstream.

The winglet twist angle plays an important role in the alleviation of the root bending moment since the twisting angle can directly reduce the local angle-of-attack on the winglet and as such shift

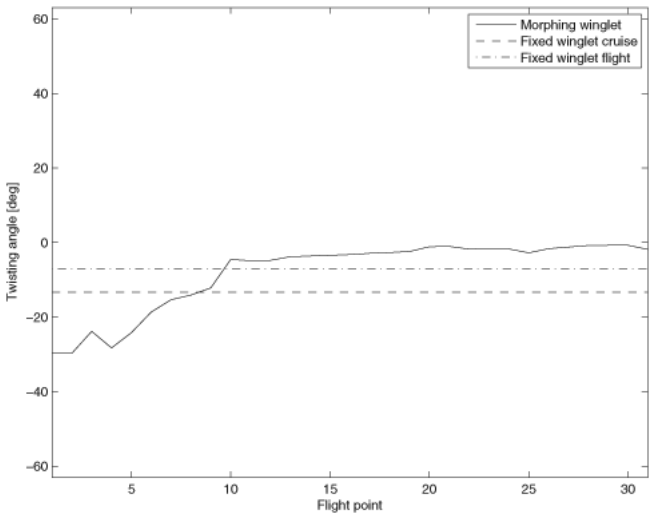

Figure 19. Change in twisting angle of the morphing winglet.

aerodynamic loading inboard. The twisting angle is the most negative, which indicates washout of the wing, at the part of the flight where the aircraft weight is the largest. Then as the moment constraint becomes more easy to satisfy because of the reduction in aircraft weight, the wing twist can also become closer to zero in order to reduce the local lift coecient and, as such, the induced and viscous drag on the winglet. The change in wing twist can be inspected in Fig. 19. The fixed winglets have a winglet twist of around 10 to 15 degrees washout. These angles seem to be rather large, but one should keep in mind that the winglet twist is not the twisting angle of the entire winglet, but the twisting difference between the two end-ribs of the winglet.

9.4 Morphing energy analysis

The energy requirement to morph the winglet is a direct consequence of the aerodynamic forces and moment acting at the winglet tip because of the fact that the winglet is modelled using one single beam element. Furthermore the skin strain energy resulting from a morphing manoeuvre influences the required morphing energy as well. It is assumed that the largest contribution from the skin straining comes from the wing shearing. There is no strain involved for wing folding since this morphing mechanism rotates wing segments rigidly with respect to each other. For wing twisting, it is assumed that this morphing mode does not strain the wing skin either, which is a safe assumption when looking at the wing twisting mechanism proposed by Vos *et al*[17].

The required energy to morph from the configuration of one flight point to the next one is calculated. The take-off position is assumed to be a straight wing, meaning all morphing angles equal to zero. The final wing position, i.e. the landing position, is again assumed to be a straight wing. The reason for both take-off and landing configurations to be straight is to maximise lift and hence minimise the corresponding speeds for noise and safety. Furthermore the morphing energy is calculated by varying the three morphing angles linearly and simultaneously from the configuration of one flight point to the one of the next flight point. Obviously the energy consumption is dependent on the order of morphing of the winglet. Therefore the results below are just exemplary and an optimisation of the morphing angle order is necessary to determine the minimal required morphing energy. This, however, is left to the detailed design of the winglet, and is therefore not included in this paper.

Wing folding is mainly dictated by the shear force in lift direction on the winglet tip. The change of the shear force in lift direction at the winglet tip, $F_{wl,z}$, over the flight is shown in Fig. 20(a).

https://doi.org/10.1017/S0001924000006461 Published online by Cambridge University Press

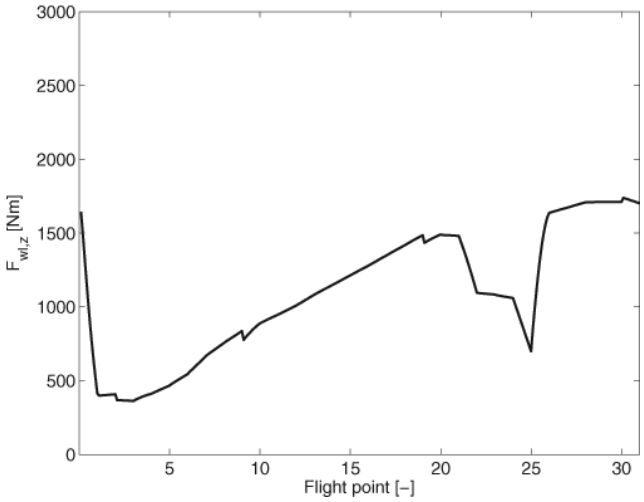

(a) Change in winglet tip shear force in lift direction over the flight

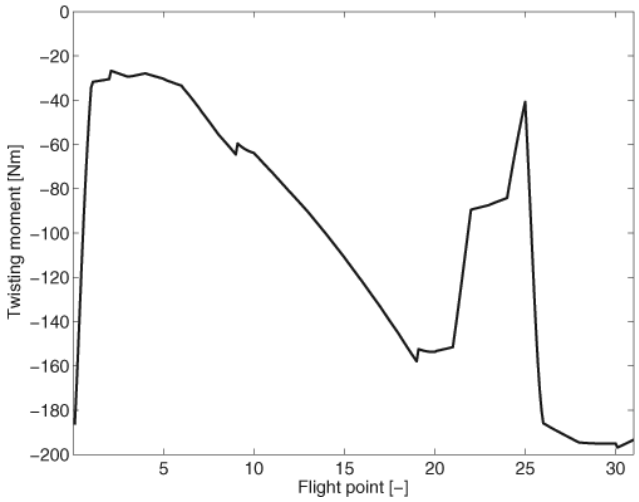

(b) Change in folding moment over the flight

Figure 20. Change in winglet shear force and corresponding folding moment.

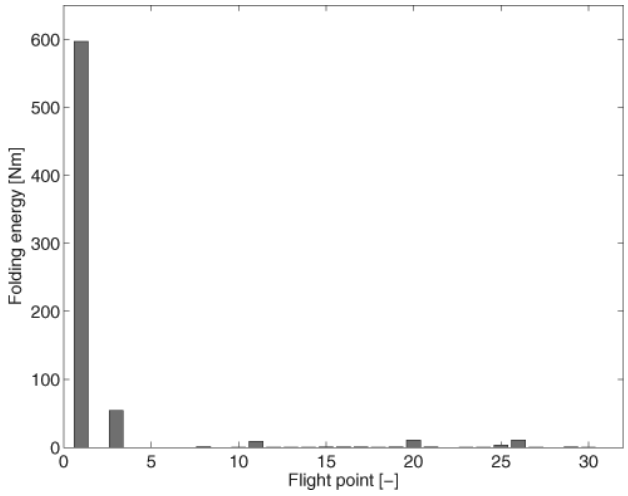

Figure 21. Required folding energy at each flight point.

It is clear from Fig 20(a) that initially the force reduces due to the sweep back and twist of the winglet, see Figs 18 and 19, respectively. Afterwards it increases again because the winglet sweeps forward and twists back to its neutral position, with the exception of the descent phase, where the force lowers temporarily due to the increase in sweep back.

In Fig. 20(b) the change of folding moment over the flight is shown. It is obvious that Figs 20(b) and 20(a) correspond qualitatively because of the aforementioned reasons. The only difference is that both figures are mirrored with respect to each other because of sign conventions.

In Fig. 21, the required energy to fold the winglet to its optimal position is shown for each flight point. Note that the largest energy is spent right after take-off to fold the winglet to the optimal climb configuration, after which the energy requirement reduces considerably. There are also flight points for which the folding energy is zero because of the fact that the aerodynamic forces aid the winglet to fold to its optimal position without the necessity of external actuator interference.

The required winglet shear moment is predominantly influenced by the drag acting on the winglet. This force acts in the direction of the flow, and is therefore assumed to aid shearing back the winglet. However, when looking at the force in global e_1^b-direction, see Fig. 2, it appears that this force is acting against a shearing back motion of the winglet. This can be inspected in Fig. 22(a).

The reason for this phenomenon is that the drag force component along the global e_1^{bf}-direction is smaller than the component of the lift in e_1^{bf}-direction. The latter is opposite to the drag component direction, and upstream in case of a positive angle-of-attack. It can be observed that the forward force decreases significantly at the first flight point. This is caused by the dump in lift due to the shearing backwards and twisting downwards of the winglet, resulting in a reduction in lift coefficient, which reduces the forward component of the lift force on the wing, and the drag component as well due to the reduction in both induced and viscous drag. The forward force is also smaller during the descent phase; again because of the lift dump due to the backward shearing of the winglet while the drag as such was smaller already because of the smaller values of the lift coecie t. However, overall, the aerodynamic force in e_1^{bf}-direction remains in forward direction, because of which the aerodynamics do not aid a downstream shear morphing motion, as also appears from Figs 22(b) and 23.

From Fig. 23 it appears that most of the shearing energy is spent during flight point 1. Also the shearing backwards at the beginning of the descent costs energy, however significantly less than for flight point 1.

The required energy to twist the winglet is comparable to the energy requirements for folding, since the needed twisting moment is determined by the aerodynamic moment around the winglet beam, which is nothing more than the lift force on the winglet multiplied by the distance between the beam and the aerodynamic centre of the wing (see Equation (14)). This trend can be observed in Fig. 24. The resulting energy requirement in Fig. 25. The analogy with the fold morphing is obvious.

The total energy consumed during the flight of all three morphing deformations is listed in Table 6 for the individual morphing angles. It is clear from the table that the energy consumption is significantly less than the energy consumption difference over the entire flight between the morphing and the fixed winglet (see Table 5), and hence, the morphing winglet is always the best solution from an energy perspective.

The above presented energy results are calculated excluding skin stiffness or morphing restraint. At the beginning of this section, it is mentioned that the largest contribution to morphing energy is the shearing of the winglet skin. The skin is assumed to be 1mm thick, and have a shear modulus of 1GPa, which is a realistic value for a

https://doi.org/10.1017/S0001924000006461 Published online by Cambridge University Press

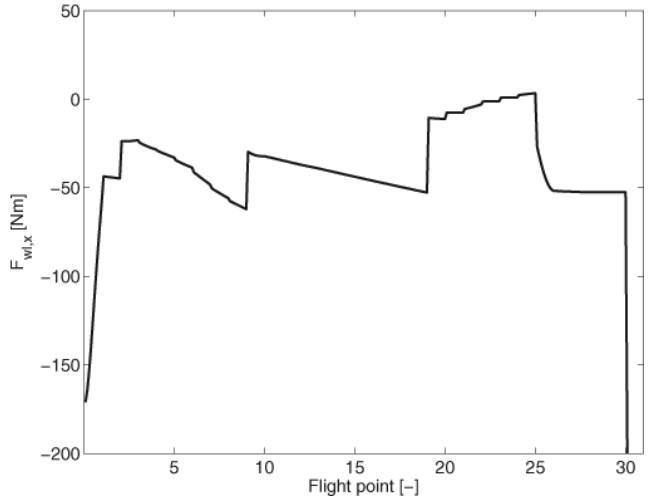

(a) Change in winglet tip shear force in drag direction over the flight

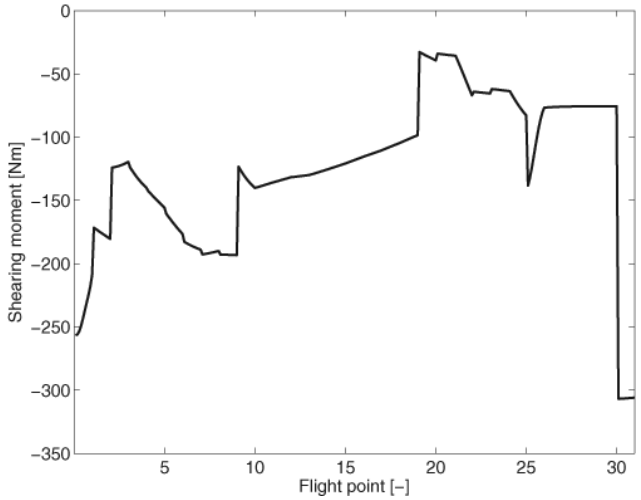

(b) Change in shearing moment over the flight

Figure 22. Change in winglet shear force and corresponding shearing moment.

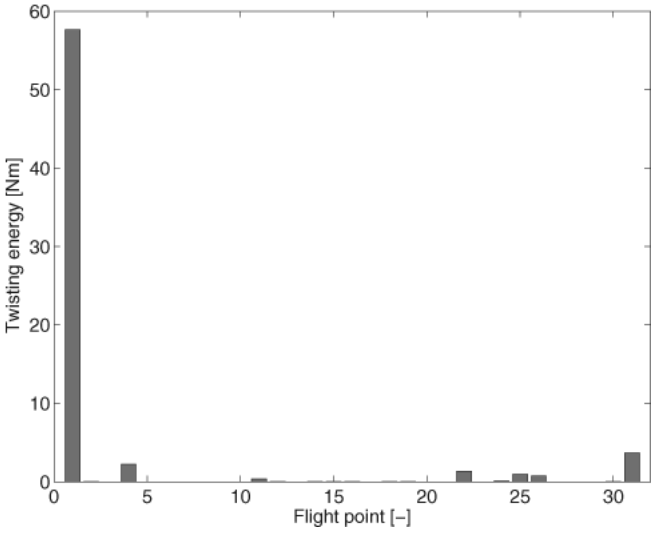

Figure 23. Required shearing energy at each flight point.

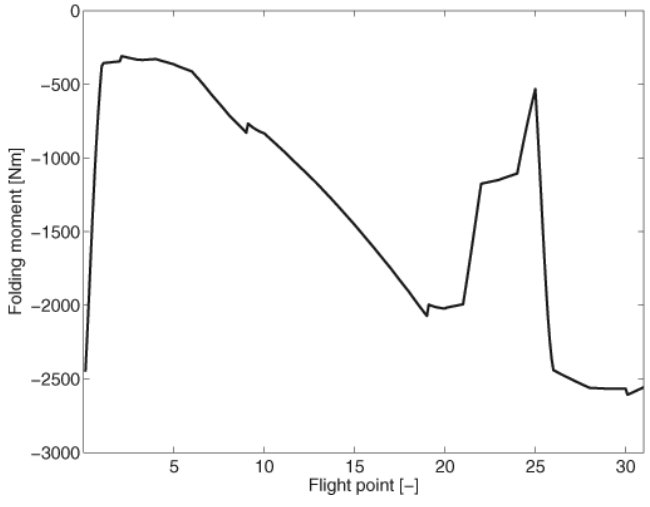

Figure 24. Change in twisting moment over the flight.

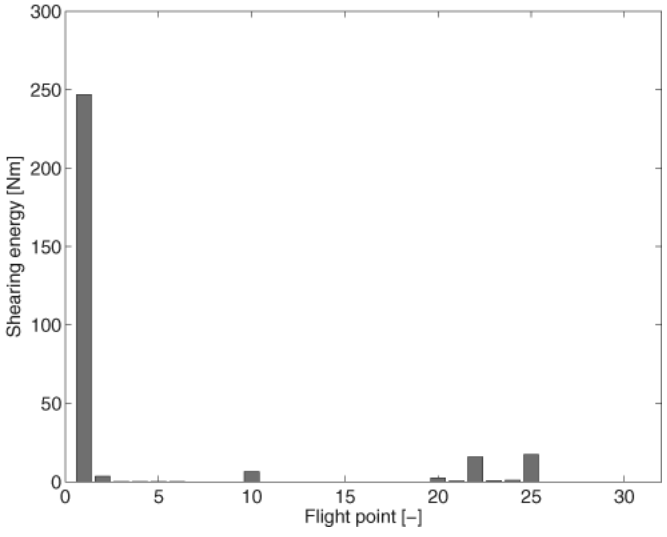

Figure 25. Required twisting energy at each flight point.

flexible skin[39]. The energy consumption of the shearing actuators for each flight point is shown in Fig. 26. The total amount of consumed energy for the shear morphing becomes $4{:}28 \times 10^6$Nm, which is 5% of the energy difference between the morphing and fixed winglet energy consumption of the total wing over the entire flight. In this case, it might be useful not to shear back during the descent phase. An amount of 44% of the total straining energy is spent on the shearing backwards during descent in exchange for less than 1% in drag reduction, as appears from Fig. 15.

The actuators effectuating the morphing manoeuvres come at a weight penalty, which affects the overall energy balance of the aircraft. An increase in total weight increases the power the engines of the aircraft have to deliver and hence add fuel and structural weight. Nonetheless, it is expected that the added weight of the actuators will be small compared to the overall weight of the existing aircraft and its systems and as such, a net reduction in total fuel carried will still result. This reduces the total take-off weight and hence further reduces the structural weight of the aircraft. Although the weight increase of the actuators is located near the wing tips, the expected increase in root-bending-moment can be cancelled by a

https://doi.org/10.1017/S0001924000006461 Published online by Cambridge University Press

Table 6
Morphing energy consumption

Morphing mechanism	Energy consumption [Nm]
Fold morphing	1,387
Shear morphing	590
Twist morphing	134

proper morphing winglet setting. Overall, it is clear that there is a system level trade-off between energy reduction due to morphing, and energy consumption and weight of the additional actuators.

10.0 CONCLUSIONS

A nonlinear aeroelastic analysis model to assess the aerodynamic, structural, and actuator performance of a morphing manoeuvre was presented in this paper. Arbitrary global morphing is achieved by discretising the morphing deformation into three distinct morphing modes; fold morphing, twist morphing, and shear morphing. The aeroelastic model consists of a corotational beam element model, which accounts for geometric nonlinearities. Furthermore a high-subsonic aerodynamic model is used, based on Weissinger's method with a Prandtl-Glauert correction for larger Mach numbers. Both the structural and aerodynamic model are closely coupled. The code mentioned above is embedded in a gradient-based optimisation routine to optimise a winglet which is retrofitted to an existing regional airliner. The design variables of this optimisation are the folding, shearing, and twisting angle of the winglet. The aim of the optimisation is to minimise the drag over the entire flight of the regional airliner. The results for the morphing winglet are compared to optimised fixed winglets. It is demonstrated that a morphing winglet outperforms a fixed winglet in the sense that the morphing winglet can improve the energy consumption reduction of a fixed winglet by a factor of two. At the part of the flight where the aircraft weight is the largest, the main objective of the winglet, next to minimising the drag, is to keep the root bending moment within limits. This is obtained by folding the winglet downwards, and creating a washout angle over the winglet. This creates a counter-acting bending moment around the wing root, while still reducing the wing induced drag. The shear of the winglet is mainly to remove wing surface area to remove viscous drag. When the wing loading decreases over the flight, the winglet extends more to maximise the aspect ratio of the wing, leading to a reduction in induced drag. Evaluation of the required energy to morph the winglet shows that the actuator energy consumption is significantly less than the energy savings because of the winglet morphing. This statement is also true if skin straining is taken into account.

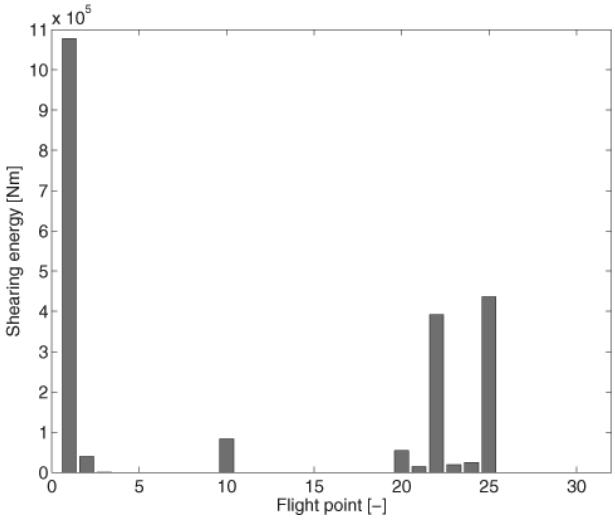

Figure 26. Required shearing energy at each flight point including skin stiffness.

REFERENCES

1. MONNER, H., SACHAU, D. and BREITBACH, E. Design aspects of the elastic trailing edge for an adaptive wing, 1999, Technical Report RTO-MP-36-14, NATO.
2. MILLER, S., VIO, G., COOPER, J., VALE, J., DA LUZ, L. and GOMES, A. *ET AL*. SMORPH — smart aircraft morphing technologies project, 2010, 51st AIAA/ASME/ASCE/AHS/ASC Structures, Structural Dynamics, and Materials Conference.
3. WLEZIEN, R., HORNE,R G., MCGOWAN, A. and PADULA, S. The aircraft morphing program, 1998, 39th AIAA/ASME/ASCE/AHS/ASC Structures, Structural Dynamics, and Materials Conference, Long Beach, CA, USA.
4. KUDVA, J. Overview of the DARPA smart wing project, *J Intelligent Material Systems and Structures,* 2004, **15**, pp 261–167.
5. SANDERS, B., CROWE, R. and GARCIA, E. Defence advanced research projects agency — smart materials and structures demonstration program overview, *J Intelligent Material Systems and Structures,* 2004, **15**, pp 227–233.
6. RODRIGUEZ, A. Morphing aircraft technology survey, 2007, 45th AIAA Aerospace Sciences Meeting and Exhibition. Reno, NV, USA.
7. BOWMAN, J., REICH, G., SANDERS, B. and FRANK, G. Simulation tool for analyzing complex shape-changing mechanisms in aircraft, 2006 AIAA Modeling and Simulation Technologies Conference and Exhibition, Keystone, CO; USA.
8. SAMAREH, J., CHWALOWSKI, P., HORTA, L., PIATAK, D. and MCGOWAN, A. Integrated aerodynamic/structural/dynamic analyses of aircraft with large shape changes, 2007, 48th AIAA/ASME/ASCE/AHS/ASC Structures, Structural Dynamics and Materials Conference, Honolulu, HI, USA.
9. REICH, G., BOWMAN, J., SANDERS, B. and FRANK, G. Development of an integrated aeroelastic multibody morphing simulation tool, 2007, 47th AIAA/ASME/ASCE/AHS/ASC Structures, Structural Dynamics and Materials Conference, Newport, RI; USA.
10. MCGOWAN, A.M.R. Overview: Morphing activities in the USA, 2008, Advanced Course on Morphing Aircraft, Materials, Mechanisms and Systems presentation.
11. DE BREUKER, R., ABDALLA, M. and GÜRDAL, Z. A generic morphing wing analysis and design framework, accepted for *J Intelligent Material Systems and Structures*, 2011.
12. WEISSHAAR, T. Morphing aircraft technology — new shapes for aircraft design, 2006, Technical Report, RTO-MP-AVT-141, NATO.
13. WIGGINS, L., STUBBS, M., JOHNSTON, C., ROBERTSHAW, H., REINHOLTZ, F. and INMAN, D. A design and analysis of a morphing hyper-elliptic cambered span (hecs) wing, 2004, 45th AIAA/ASME/ASCE/AHS/ASC Structures, Structural Dynamics and Materials Conference, Palm Springs, CA; USA.
14. URSACHE, N.M., MELIN, T., ISIKVEREN, A.T. and FRISWELL, M.I. Morphing winglets for aircraft multi-phase improvement, 2007, Seventh AIAA Aviation Technology, Integration and Operations Conference (ATIO).
15. CESNIK, C.E.S and BROWN, E.L. Active warping control of a joined-wing airplane configuration, 2003, 44th AIAA/ASME/ASCE/AHS/ASC Structures, Structural Dynamics and Materials Conference.
16. MAJJI, M., REDINIOTIS, O.K. and JUNKINS, J.L. Design of a morphing wing: modeling and experiments, 2007, AIAA Atmospheric Flight Mechanics Conference and Exhibition.
17. VOS, R., GRDAL, Z. and ABDALLA, M. Mechanism for warp-controlled twist of a morphing wing, *J Aircr*, 2010, **47**, (2), pp 450-457.
18. MAUTE, K., REICH, G. and SANDERS, B. In-plane morphing designs by topology optimization, 2003, 16th International Conference on Adaptive Structures and Technologies.
19. SIMMONS, F. and FREUND, D. Morphing concept for quiet supersonic jet boom mitigation, 2005, 43rd AIAA Aerospace Sciences Meeting and Exhibition.
20. INOYAMA, D., SANDERS, B.P. and JOO, J.J. Conceptual design and multi-disciplinary optimization of in-plane morphing wing structures, 2006, SPIE Conference on Smart Structures and Materials, pp 61-66.

https://doi.org/10.1017/S0001924000006461 Published online by Cambridge University Press

21. PATIL, M. and HODGES, D. On the importance of aerodynamic and structural geometrical nonlinearities in aeroelastic behavior of high-aspect-ratio wings, 2000, 41st AIAA/ASME/ASCE/AHS/ASC Structures, Structural Dynamics and Materials Conference.
22. CRISFIELD, M. A consistent co-rotational formulation for non-linear, three-dimensional, beam-elements, *Computer Methods in Applied Mechanics and Engineering*, 1990; **81**, pp 131–50.
23. WEMPNER, G. Finite elements, finite rotations and small strains of flexible shells, *Int J of Solids and Structures*, 1969, **5**, pp 117–53.
24. CRISFIELD, M. *Non-linear Finite Element Analysis of Solids and Structures*, Vol 2, 1991, John Wiley & Sons, UK.
25. BATTINI, J.M. and PACOSTE, C. Co-rotational beam elements with warping effects in instability problems, *Computer Methods in Applied Mechanics and Engineering*, 2002; **191**, pp 1755–89.
26. RIVELLO, R. *Theory and Analysis of Flight Structures*, 1969, McGraw-Hill, USA.
27. WEISSINGER, J. The lift distribution of swept-back wings, 1947, Technical Memorandum 1120; NACA.
28. JONES, R. and COHEN, D. *High Speed Wing Theory*, 1960, Vol 6 of Princeton Aeronautical Paperback, Princeton University Press, NJ; USA.
29. ANDERSON, J. *Fundamentals of Aerodynamics*, Second edition, 1991, New York: McGraw-Hill Internation Editions.
30. KATZ J. and PLOTKIN, A. *Low-Speed Aerodynamics*, Second edition, 2001, Aerospace Series; Cambridge University Press.
31. GUERMOND, J.L. A generalized lifting-line theory for curved and swept wings, *J Fluid Mechanics*, 1990, **211**, pp 497–513.
32. ABBOTT, I., VON DOENHO, A. and STIVERS L.S.J. Summary of airfoil data, 1945, Technical Report 824, NACA.
33. CRISFIELD, M. *Non-linear Finite Element Analysis of Solids and Structures*, Vol 1, 1991, John Wiley & Sons, UK.
34. STREIT, T., HIMISCH, J., HEINRICH, R., NAGEL, B., HORSTMANN, K. and LIERSCH, C. Design of a retrofit winglet for a transport aircraft with assessment of cruise and ultimate structural loads, *Notes on Numerical Fluid Mechanics*, 2007, **96**, pp 62–70.
35. PRANANTA, B., NAMER, A., MASELAND, J., VAN MUIJDEN, J. and SPEKREIJSE, S. Winglets on large civil aircraft: impact on wing deformation, 2005, Technical Report NLR-TP-2005-366, National Aerospace Laboratory NLR.
36. SVANBERG, K. The method of moving asymptotes — a new method for structural optimization, 1987, **24**, pp 359–73.
37. SVANBERG, K. A class of globally convergent optimization methods based on conservative convex separable approximations 2002, **12**, (2), pp 555–73.
38. LAZOS, B. and VISSER, K. Aerodynamic comparison of hyper-elliptic cambered span (hecs) wings with conventional configurations, 2006, 24th AIAA Applied Aerodynamics Conference, San Francisco, CA, USA.
39. MURRAY, G., GANDHI, F. and BAKIS, C. Flexible matrix composite skins for one-dimensional wing morphing. *J Intelligent Materials Systems*, 2010, **21**, pp 1771–81.

https://doi.org/10.1017/S0001924000006461 Published online by Cambridge University Press